Nanoscale

PAPER

View Article Online
View Journal | View Issue

Cite this: *Nanoscale*, 2023, **15**, 8662

Tuning innate immune function using microneedles containing multiple classes of toll-like receptor agonists†

Camilla Edwards, [a] Robert S. Oakes [a,b] and Christopher M. Jewell *[a,b,c,d,e]

Microneedle arrays (MNAs) are patches displaying hundreds of micron-scale needles that can penetrate skin. As a result, these arrays efficiently and painlessly access this immune cell-rich niche, motivating significant clinical interest in MNA-based vaccines. Our lab has developed immune polyelectrolyte multilayers (iPEMs), nanostructures built entirely from immune signals employing electrostatic self-assembly. iPEMs consist of positively charged peptide antigen and negatively charged toll-like receptor agonists (TLRas) to assemble these components at ultra-high density since no carrier is needed. Here we used this technology to deliver MNAs with antigen and defined ratios of multiple classes of TLRa. Notably, this approach resulted in facile assembly and corresponding signal transduction through each respective TLR pathway. This control ultimately activated primary antigen presenting cells and drove proliferation of antigen-specific T cells. In related *in vivo* vaccine studies, application of MNAs resulted in distinct T cells response depending on the number of TLRa classes delivered with MNAs. These MNAs technologies create an opportunity to deliver nanostructured vaccine components at high density, and to probe integration of multiple TLRas in skin to tune immunity.

Received 21st January 2023,
Accepted 19th April 2023

DOI: 10.1039/d3nr00333g

rsc.li/nanoscale

Introduction

Vaccines are an important technology to prevent and stop the spread of global disease. These technologies harness the body's natural defense mechanisms against pathogens and require integration of multiple signal classes to drive efficient, protective responses while avoiding attack of self-tissues.[1–3] Exciting clinical studies show that delivering combinations of adjuvants – for example, toll-like receptor agonists (TLRas) – can improve and tailor vaccine responses.[4,5] TLRs and other innate immune sensor systems are expressed at high levels on antigen presenting cells, many of which are concentrated in the skin. Because of this unique niche, arrays of micron-scale needles – termed microneedle arrays (MNAs) – have emerged as technologies that directly target this immunological niche without reaching pain receptors.[6,7] Here we create a tunable MNA platform for combinatorial control over innate signaling by delivering antigen with precise ratios of multiple classes of TLRas.

Vaccines drive efficient and protective responses against dynamic pathogens while maintaining selectivity to avoid side effects or autoimmunity. These goals are accomplished by including multiple signal classes, including (i) antigen – specific proteins or peptide fragments from pathogens that confer specificity, and (ii) adjuvant, which stimulate responses by activating antigen-presenting cells (APCs) and functional cells such as lymphocytes. APCs are concentrated in locations that commonly encounter foreign pathogens; for example, skin and mucosal layers.[8–11] After encountering antigen, APCs migrate to specialized immune organs known as lymph nodes to co-present antigen and specific costimulatory markers to naïve cells, specifically T and B lymphocytes. Integration of these signals by lymphocytes results in proliferation and maturation, allowing the now antigen-experienced effector cells to return to the periphery to destroy foreign pathogens displaying the antigen.[12]

APCs express high levels of toll-like receptors (TLRs) internally and on the cell surface. These receptors detect molecular patterns common in pathogens, but not in mammalian cells; thus, these TLR agonists (TLRas) trigger TLR danger sensing pathways.[13–15] For this reason, TLRas are attractive candidates

[a]*Fischell Department of Bioengineering, University of Maryland, College Park, MD 20742, USA. E-mail: cmjewell@umd.edu*
[b]*United States Department of Veterans Affairs, VA Maryland Health Care System, Baltimore, MD 21201, USA*
[c]*Robert E. Fischell Institute for Biomedical Devices, College Park, MD 20742, USA*
[d]*Department of Microbiology and Immunology, University of Maryland Medical School, Baltimore, MD 21201, USA*
[e]*Marlene and Stewart Greenebaum Cancer Center, Baltimore, MD 21201, USA*

†Electronic supplementary information (ESI) available: Detailed cargo loading analysis, flow cytometry gating schemes, cell viability, and measurements at additional time points for TLR assays. See DOI: https://doi.org/10.1039/d3nr00333g

for adjuvants to increase the immunogenicity of vaccine antigens.[16–19] As one salient illustration, mRNA and adenovirus vector COVID-19 vaccines both contain TLRas – either the mRNA itself or as a component of the vector – serving as crucial components to drive effective response against COVID antigens through initiation of innate signaling.[20] One emerging strategy to improve vaccine outcomes is the incorporation of multiple classes of TLRas. For example, a cancer vaccine integrating TLR4a/TLR9a is significantly more effective at driving long-lasting clinical responses than an equivalent vaccine containing only TLR4a.[21] These and other studies demonstrate vaccines that target multiple pathways have great potential to tune immune responses and improve outcomes.[22–24]

MNAs offer exciting opportunities to improve both vaccine potency and administration. MNAs directly target the APC-rich dermal layers of the skin without reaching pain receptors, making MNAs attractive for vaccine delivery relative to conventional, needle-based approaches. These arrays come in a variety of designs, including coated, dissolvable, hollow, and solid; each with its own benefits regarding dosing, kinetics, and cargo stability.[25–27] However, these designs share several key advantages relative to traditional needle-based vaccine administration. MNAs reduce pain at the site of injection because the needle length scale it too short to reach pain receptors. Additionally, MNAs are not medical sharps and can reduce the need for a tightly regulated cold chain when arrays are shipped with components contained within the needle or coated onto the surface.[28,29] These problems are underscored by distribution challenges ubiquitous to many developing regions.[30–32] Immunologically, specialized APCs such as Langerhans and dendritic cells (DCs) are concentrated in the skin, creating a unique niche for vaccination.[27,33–35] These features have driven considerable clinical exploration. For example, dissolvable microneedles have been studied in phase 1 trials to deliver influenza vaccines in humans and are being explored in therapeutic vaccination for cancer or other diseases.[36–38]

Our lab has developed MNAs as a substrate for self-assembly of immune signals at high density.[12,35,39–41] In particular, we recently reported electrostatic assembly of model antigen with a TLR agonist using electrostatics to form immune polyelectrolyte multilayers (iPEMs).[12,42] These assemblies load components in a simple, low energy format without need of a carrier or matrix. Thus, 100% of the formulation is cargo, maximizing signal density. Further, because there are no polymeric carriers in the structures, there are no complicating background effects resulting from the intrinsic immunogenicity of many synthetic polymers.[43,44] Here, we develop this idea as a platform for combinatorial delivery of multiple TLRas. We created a library from peptide antigens and defined ratios of TLR3a and TLR9a. Specifically we used polyinosinic-polycytidylic acid (polyIC), a synthetic double stranded RNA, as our TLR3a. We used CpG oligonucleotide – a synthetic single-stranded DNA molecule, as our TLR9a. We show that combinations of antigen and distinct classes of TLRas can be assembled on MNAs and used to control the relative composition of these self-assembled immune nanostructures. Importantly, the TLRa composition defines the simultaneous and corresponding levels of TLR signaling in each cognate TLR pathway. These events lead to activation of primary APCs and expansion of antigen-specific T cells. Using a simple mouse vaccine model, we show MNAs generate antigen-specific T cell responses; notably, the magnitude depends on the number of TLRa classes delivered with MNAs. This work provides a platform for integrating antigens and combinations of TLRas to tune innate immune signaling for specific vaccine and immunotherapy applications targeting the skin niche.

Experimental section

Materials

SIINFEKL, a model antigen derived from ovalbumin, and SIINFEKL appended with 9 arginine residues (SIINFEKL R9) as a cationic tag to support assembly were synthesized by Genscript with >98% purity; peptides were synthesized with or without a FITC label on the N-terminus. Low molecular weight polyIC was purchased from Invivogen. TLR9 agonist CpG oligonucleotide (5′T*C*C*A*T*G*A*C*G*T*T*C*C*T*G*A*C*G*T*T3′) was synthesized by IDT with a phosphorothioate backbone. Label-IT nucleic acid labeling kits (Cy3 and Cy5) were purchased from Mirus Bio LLC. PolyIC and CpG were labeled according to the Mirus Bio instructions. Poly(L-lactide) (PLLA) was purchased from Sigma-Aldrich. A Sylgard silicone elastomer kit was obtained from Dow Corning.

Animals and care

C57BL/6J and C57BL/6-Tg(TcraTcrb)1100Mjb/J mice (female, 6–8 weeks) were obtained from The Jackson Laboratory. All animal care and experiments were carried out using protocols approved and overseen by the University of Maryland IACUC committee in compliance with local, state, and federal guidelines.

MN fabrication

MN arrays were prepared as previously described.[45] Briefly, poly(dimethylsiloxane) (PDMS) molds using a Sylgard 184 silicon elastomer kit (Dow-Corning) were prepared using a Clark-MXR-CPA-2010 (VaxDesign). PLLA was melted through a phase transition in the molds under vacuum (−25 in. Hg, 200 °C, 40 min), then cooled to −20 °C for least 30 min before separating the cast PLLA MNAs from the PDMS mold. MN morphology of coated and uncoated arrays were characterized by scanning electron microscopy (SEM) using a JEOL 6700F FEG-SEM.

Assembly and characterization of iPEMs on MNAs

All bilayers (BL) were assembled using a DR3 dipping robot (Riegler & Kirstein GmbH). PLLA MNAs were cleaned *via* ethanol rinsing, dried under filtered air, and charged with an oxygen plasma deposition system (Jupiter III, March). The prepared arrays were then sequentially exposed for 5 min each to

FSIIN* (1 mg mL^{-1}, 0.2 M sodium acetate buffer) and varying combinations of TLR9a and TLR3a (1 mg mL^{-1}, 0.2 M sodium acetate), with or without Cy3/Cy5 labels, except where noted in text. These deposition steps were separated by two sequential 1 min rinsing steps in deionized water, with fresh rinse solutions used for each cycle. Assembly on MNs was automated using a DR3 dipping robot programmed to repeat the bilayer deposition a desired number of times, up to 64 BL (128 layers).

Quantification of FSIIN*, TLR3a (PolyIC), and TLR9a (CpG)

MNA Cargo was removed from the needles using RNA Lysis Buffer. Cargo was eluted through spin columns, and the amount of FSIIN* was determined by measuring the absorbance at 482 nm and comparing to a standard curve made with known amounts of FSIIN*. Next, deionized water was used to elute the TLR3a from the same spin columns. This amount was determined by measuring the absorbance at 280 nm and comparing to a standard curve. Finally, a portion of the initial elution was mixed with oligo binding buffer and eluted again through a fresh spin column. Deionized water was used to elute the TLR9a from the column, and its absorbance was measured at 282 nm and similarly compared to a standard curve. Standard curves were developed by combining known amounts of TLR3a, TLR9a, and FSIIN* in soluble solutions, then running through columns to ensure each component could be independently detected (see Fig. S1†). Measurement wavelengths (*i.e.* 482 nm, 280 nm, and 282 nm for FSIIN*, TLR3a, and TLR9a respectively) were determined by performing UV Vis line scans and using the peak maximum wavelength. All buffers and columns were obtained from the Zymo Research Corporation.

MNA imaging

Confocal microscopy (Olympus FLUOVIEW FV3000) was used to visualize fluorescently labelled SIINFEKL R9 (FITC), TLR3a, and TLR9a (Cy3 and Cy5) on MNAs and individual needles. To analyze pixel intensity across different combinations, lines centered in the middle of the needle and spanning the diameter of each needle were drawn. Then, the pixel intensity of pseudo-colored TLR3a, TLR9a, and FSIIN* was measured. This was repeated for 36 lines, spanning the entire circumference of the needle. Dynamic range was calculated for each point by dividing the signal for a given point by the maximum signal minus the minimum signal for that needle. Averages of this range were plotted as a function of distance along the axis.

In vitro DC studies

Splenic DCs were isolated from C57BL/6 mice with CD11c positive magnetic isolation kit (Miltenyi Biotec) following the manufactuer's protocol. After isolation, the cell pellet was resuspended in 1 mL of DC medium (RPMI1640, 10% FBS, 0.5% pen/strep, 50 μM 2-mercaptoethanol (2-ME)) prior to use. 1×10^5 DCs in 200μL were plated on top of a quarter of a MNA in each well in a 96 well plate. Untreated DCs, soluble peptide FSIIN* (5 μg mL^{-1}, 1 μg per well), TLR3a (10 μg mL^{-1}, 2 μg per well), TLR9a (10 μg mL^{-1}, 2 μg per well), or co-treatment with FSIIN* (5 μg mL^{-1}, 1 μg per well), TLR3a (10 μg mL^{-1}, 2 μg per well), and TLR9a (10 μg mL^{-1}, 2 μg per well) were used as controls in *in vitro* studies. Soluble control amounts were selected based on previous experiments to provide activation of cells; because not all MNA cargo dissolved into solution (as evidenced by visible FITC SIINFEKL on needles), soluble doses are less than the total amount of cargo on needles. Comparisons are noted in the text.

After 24 h, flow cytometry was used to assess DC maturation. Briefly, cells were washed with 200 μL of FACS buffer (1% BSA in PBS), collected by centrifugation, then blocked with anti-CD16/32 (BD Biosciences) prior to surface marker staining. To assess DC maturation, DCs were stained for CD40 (PE, BD Biosciences), CD80 (APC, BD Biosciences), CD86 (V450, BD Biosciences), SIINFEKL presented in MHC1 (PECy7, Biolegend), and viability (Invitrogen). Samples were analyzed *via* flow cytometry (Cytoflex, BD) and FlowJo v10. FlowJo software was used for all data analysis.

In vitro $CD8^{\pm}$ T cell expansion

CD11c-enriched DCs were isolated and treated with MNA quarters as described above. Positive and negative control wells received free SIINFEKL peptide (2 μg mL^{-1}) or no peptide, respectively. After an additional 24 h, $CD8^+$ T cells were isolated from OT-I mice using a $CD8^+$ negative selection isolation kit from Stemcell. The purified cells were washed twice to remove any serum and labeled with 5 μM of a carboxyfluorescein succinimidyl ester (CFSE) proliferation dye (eFluor 670; eBioscience) for 10 min at 37 °C in the dark. After 10 min, the dye was neutralized with 5 times the volume of T cell medium (RPMI11640, 10% FBS, 1× nonessential amino acids, 10 mM HEPES, 2 mM L-glutamine, 0.5% penicillin streptomycin, 50 μM 2-ME) followed by washing three times with T cell medium. The resulting cells (3×10^5 cells/50 μL) were added into the wells containing DCs/MNA array pieces and DCs/controls, then incubated for 48 h. After incubation, cells analyzed for proliferation. To assess T cell proliferation, cells were first blocked with anti-CD16/32 as described above and stained with anti-CD3 (PE-Cy7, BD Biosciences) and anti-CD8a (APC, BD Biosciences) for $CD8^+$ T cells. Flow cytometry was used to analyze the signal of eFluor 450 dye as an indication of fluorescence dilution resulting from T cell proliferation.

TLR reporter cell studies

To assess the kinetics of TLR3- and TLR9-specific signaling, HEK-Blue mTLR3 or HEK-Blue mTLR9 reporter cells (InvivoGen) were plated at 5×10^5 cells per well in HEK-Blue Detection medium (InvivoGen) per the manufacturers' instructions. Cells were treated with MNA quarters, soluble TLR3a (10 μg per well), soluble TLR9a (10 μg per well), soluble FSIIN* (10 μg per well) or soluble TLR3/9a (5 μg PolyIC + 5 μg CpG per well) for 10 to 16 hours. The TLR3 and TLR9 reporter cells have different kinetics; in the main text, we report the absorbance at the appropriate time scale for each type of reporter cell, while the corresponding absorbance for the time point of the other reporter cell is included in the ESI (Fig. S2†).

Absorbance was measured hourly at 620 nm using a Tecan fluorescence microplate reader. Results are shown relative to media only absorbance.

ELISA assays

Supernatants from cocultures of splenic DCs and transgenic $CD8^+$ T cells were quantified by sandwich ELISA according to the manufacturer's protocols for the secretion of IFN-γ (BD Biosciences).

In vivo vaccination studies using electrostatically-assembled MNAs

C57Bl/6 mice (n = 4 per group) were immunized using the same vaccine components and a related MNA design. To form these MNAs, vaccine components were first electrostatically complexed together *via* mixing (70 μg FSIIN* and 100 μg total TLRa, at the indicated ratios), then centrifuged into the tips of PDMS MNA molds. Then, cold water fish gelatin (Sigma) was backfilled behind complexes. Arrays were allowed to dry for 36 h and de-molded to form dissolvable, complex-loaded MNAs. Mice were immunized with these dissolvable MNAs on day 0 on the right flank by using a modified nail punch to ensure needles had entered skin. Needles were allowed to dissolve and MNAs were allowed to naturally detach from the mouse flank. Blood was then collected by the submandibular route on day 7. Blood samples were treated with 1 mL of ACK lysing buffer (Life Technologies) to remove red blood cells, collected by centrifugation (500*g*, 5 min), washed in FACS buffer, and collected. Each cell sample was then blocked with anti-CD16/32 for 10 min at RT, followed by staining with the MHC I SIINFEKL tetramer (PE-conjugated, NIH tetramer core) for 30 min at RT. Cells were subsequently surface-stained by incubation with anti-CD8a (APC, BD bioscience) and for viability (near infrared dye, Invitrogen) for 20 min at RT, washed twice, and suspended in FACS buffer for analysis by flow cytometry.

Statistical analysis

Data was analyzed by multiple group comparison using one-way analysis of variance (ANOVA) with a Tukey post-test in GraphPad Prism v.6.02. Statistical significance was defined at p values < 0.05 (95% confidence interval) and indicated as * = $p \leq 0.05$, ** = $p \leq 0.01$, *** = $p \leq 0.001$, and **** = $p \leq 0.0001$.

Results and discussion

Electrostatic assembly allows controllable loading and linear growth

To establish a route for electrostatic assembly of TLRa on MNs, we began with a simple design using TLR3a (PolyIC) and model antigen (SIINFEKL). To prepare coated MNAs, PLLA-cast MNAs were dip-coated using sequential assembly steps (Scheme 1). Since the peptide antigen is positively charged and the nucleic acid TLRa is negatively charged, these components serve as both immunological cues and structural components for assembly by electrostatic interactions. SEM images revealed the coated MNA displayed conformal coatings that maintained the geometric fidelity of the MNA substrate even after depositing 64 bilayers, matching the geometry of uncoated needles before dipping. A representative image of the uncoated needle is shown in Fig. 1A. Visualization of coatings assembled with fluorescently labeled SIINFEKL-R9 (FITC) and TLR3a (Cy3) using laser scanning confocal microscopy revealed co-localization of signal. Although the entire surface was coated, more intense signal was observed in some regions near the MNA tips (Fig. 1B). This could result from dipping and drying during the robotic dip-coating process. However, quantification of loading revealed facile control over the loading of each component, proportional to the number of layers deposited (Fig. 1C). A linear relationship was observed between the number of adsorption steps and the amount of cargo deposited (Fig. S3†). To confirm loading was driven by electrostatic interactions on these MNAs substrates – and not other interactions, such as protein-nucleic acid entanglements – we performed another study using the same process but omitting the TLRa from the second dipping solution. Exclusion of the TLRa component eliminated growth (Fig. 1D), indicating the need for the opposite charged TLRas component to support growth on the MNA.

Electrostatic assembly of immune signals allows modular coating of MNAs with control over the relative composition of TLRa.

We next tested if the assembly and relative concentrations of multiple classes of TLRas with antigen could be controlled on MNAs. In these studies, the total antigen and adjuvant (*i.e.* TLRas) concentrations were fixed, while the relative concentration of distinct TLRa classes – TLR3a and TLR9a – was varied (*i.e.*, TLRa ratio).

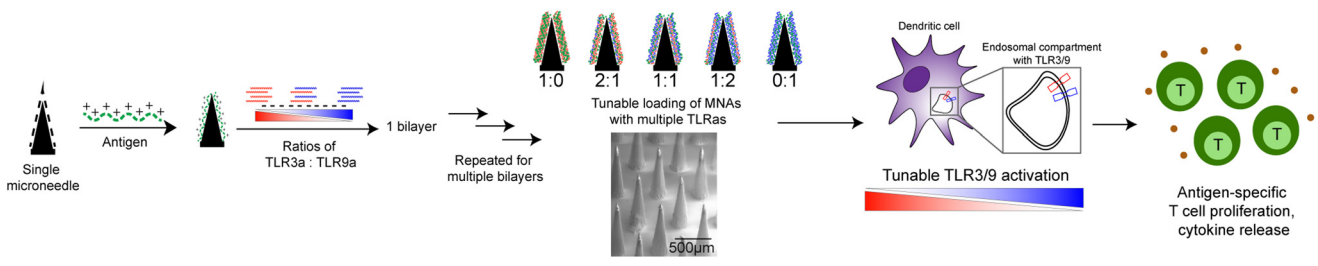

Scheme 1 Tunable loading and composition of MNAs drives DC activation and effector cell response.

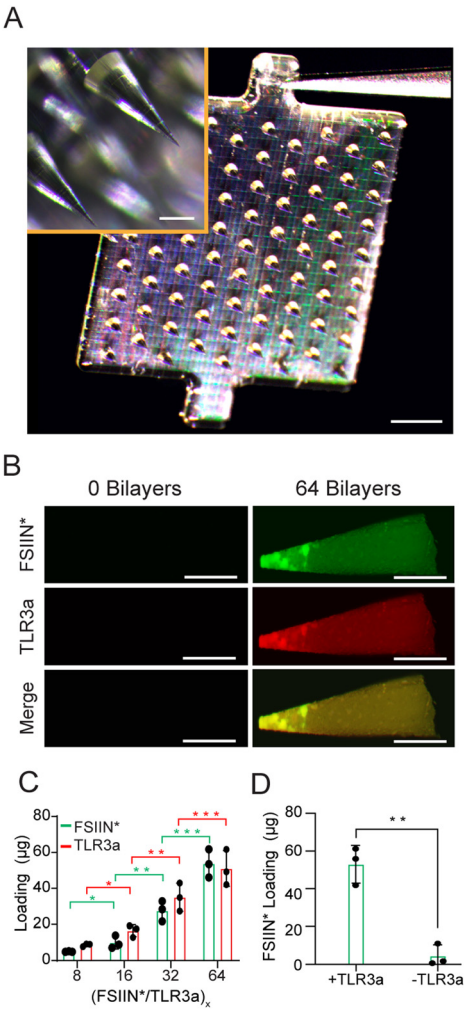

Fig. 1 Microneedle loading is driven electrostatically, can be controlled, and has a linear growth regime. (A) Microneedles, small patches of needles too short to reach pain receptors but long enough to deliver coatings to the dermal layers, can be formed out of PLLA plastic. Scale bar = 1 mm. (B) Confocal microscopy Z-stack images of individual needles coated with 64 BL of FSIIN* (green) and TLR3a (red). Scale bar is 100μm. (C) Direct loading measurements of FSIIN* and TLR3a on MNAs. (D) FSIIN* loaded onto microneedles with (left) or without (right) the presence of TLR3a. Data are presented as mean ± SD.

Laser scanning confocal microscopy revealed constant levels of antigen deposition, while the relative levels of TLR3a and TLR9a corresponded to the defined TLRa assembly ratio. This was evident in both cross sections (Fig. 2A) and maximum intensity projections (Fig. 2B). Image analysis revealed co-localization of signal, with intensity levels controlled by the input TLRa ratio (Fig. 2C). This point was underscored by the maximum of the dynamic range for each TLRa (Fig. 2D). Analytical quantification of the amount of each component loaded confirmed control over the absolute and relative concentrations of antigen and TLRas (Fig. 2E and Fig. S3†). These studies resulted in a library of MNAs comprising five different ratios of TLR3a to TLR9a, while maintaining constant antigen.

The amount of immune signals assembled on MNAs controls DC activation and cargo uptake

Beginning with the 1 : 1 TLR3a : TLR9a MNA design, we first tested if the level of cargo loading altered antigen uptake and presentation by primary DCs, as well as the presentation of key costimulatory markers on APCs involved in T cell expansion (*i.e.*, CD80, CD86, CD40). Cells were plated directly onto quarters of the arrays, as previous studies in our lab showed that iPEM- coated MNAs delivered components to the dermal layers of murine skin.[12] Thus, for these *in vitro* studies, we hypothesized that DCs would be able to take up cargo from the arrays or from the dissolution of components in solution. While the needles themselves would promote this uptake *in vivo* in the skin, we did not expect the needles to directly penetrate the cells to deliver cargo. Additionally, upon completion of the studies, not all cargo had been released into solution; thus, the mass of soluble control treatment was selected to be less than that of the total amount delivered in solution. Using a common gating scheme (Fig. S4A†) and nuclear dye, we assessed viability (Fig. S4B†). These studies confirmed MNA – coated and uncoated – did not significantly alter cell viability, regardless of the number of BLs deposited, although uncoated needles and 64BL needles did result in lowered viability of one of the samples. Despite these slight reductions, there were enough cells to analyze surface markers and antigen uptake and presentation across all groups. Next, we treated cells with needles coated with defined numbers of BLs. In these studies, antigen internalization – indicated by FITC signal, generally increased with increasing numbers of bilayers (Fig. 3A and B), with 64BL-coated MNAs causing DCs to take up statistically similar amounts of FSIIN* to soluble controls (statistics not included on graph for the sake of clarity). This internalization led to processing and presentation of SIINFEKL antigen in MHC-I machinery in a manner that correlated with the number of BLs deposited (Fig. 3C and D). Here, 32 and 64BL-coated MNAs caused DCs to express SIINFEKL in MHC-I at similar levels to DCs treated with soluble mixtures of components (statistics not included on graph for the sake of clarity). Interestingly, although this parameter generally increased with the number of BLs, moving from 8BL to 16BL did not cause a significant increase at the timescale analyzed. This may indicate the assay is not sensitive enough to resolve the smaller difference in loading between 8 BL and 16 BL, relative to larger changes in loading moving from 16 BL to 32 BLs. Studies with additional increments between numbers of bilayers, along with kinetic analysis, could provide further insight into the antigen uptake and display kinetics. It is also important to note that solid 64BL surface coatings on MNAs were able to induce a similar response to soluble controls (although soluble control dosing amounts were lower than the amount coated onto the needle). *In vivo*, these components on these needles would be able to penetrate the skin and deliver cargo to dermal immune cells. Thus, these findings providing exciting motivation for delivery of these components through the skin. Increased antigen uptake and presentation leads to

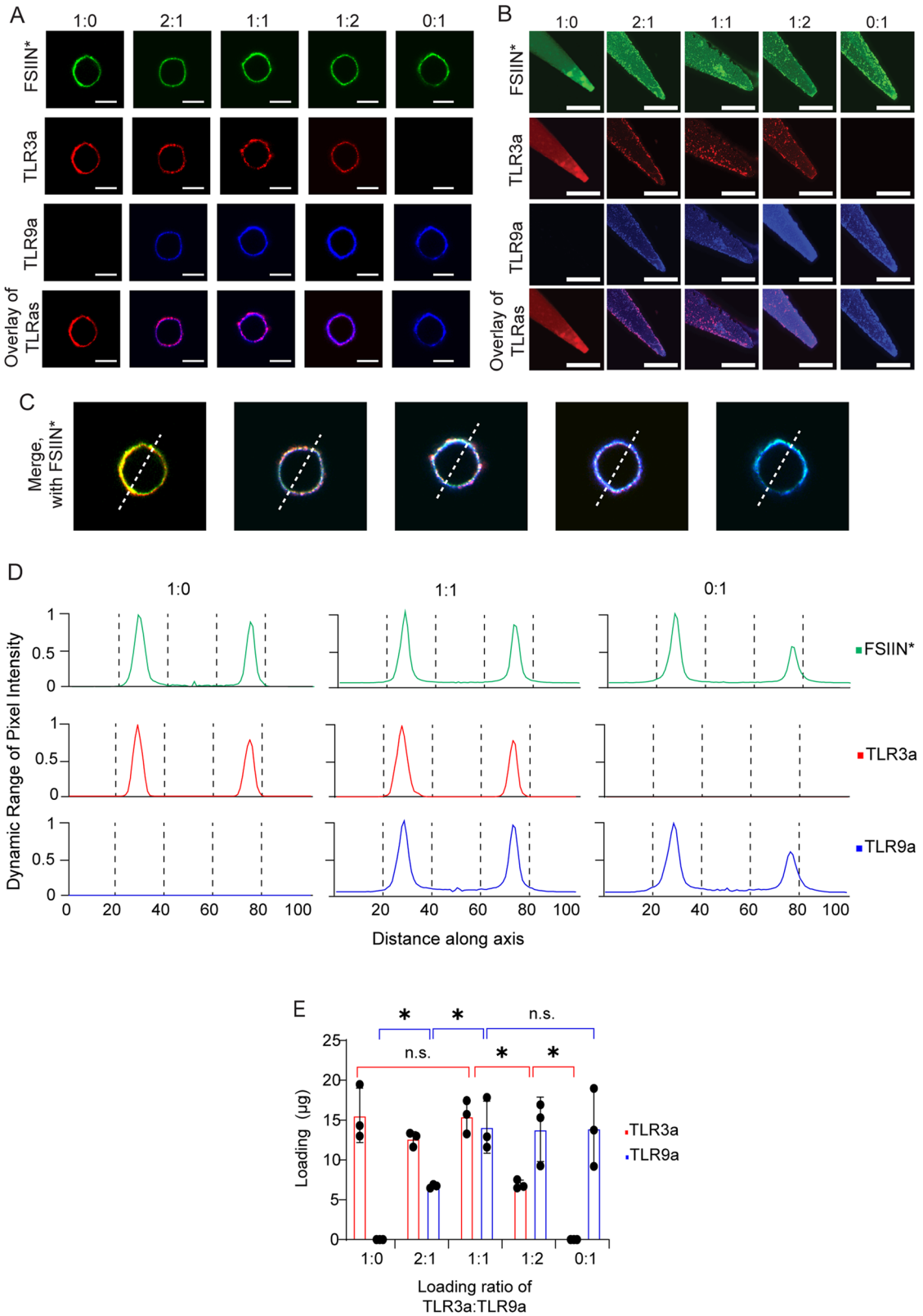

Fig. 2 Multiple TLRas can be loaded onto microneedles uniformly and in defined ratios. Confocal microscopy (A) slices of arrays and (B) needle Z stack projections at varying compositions. (C) FSIIN*, TLR3a, and TLR9a merged slices of arrays, with representative line to show image analysis technique. (D) Lines in C were rotated through each cross section to obtain 36 measurements, then averaged and analyzed to calculate the dynamic range of pixel intensity. Dynamic range was calculated for each point by dividing the signal for a given point by the maximum signal minus the minimum signal for that cross section. (E) Direct loading measurements of combinatorial MNAs, showing that the relative amount of TLR3a to TLR9a can be varied. All scale bars are 100μm. Data are presented as mean ± SD.

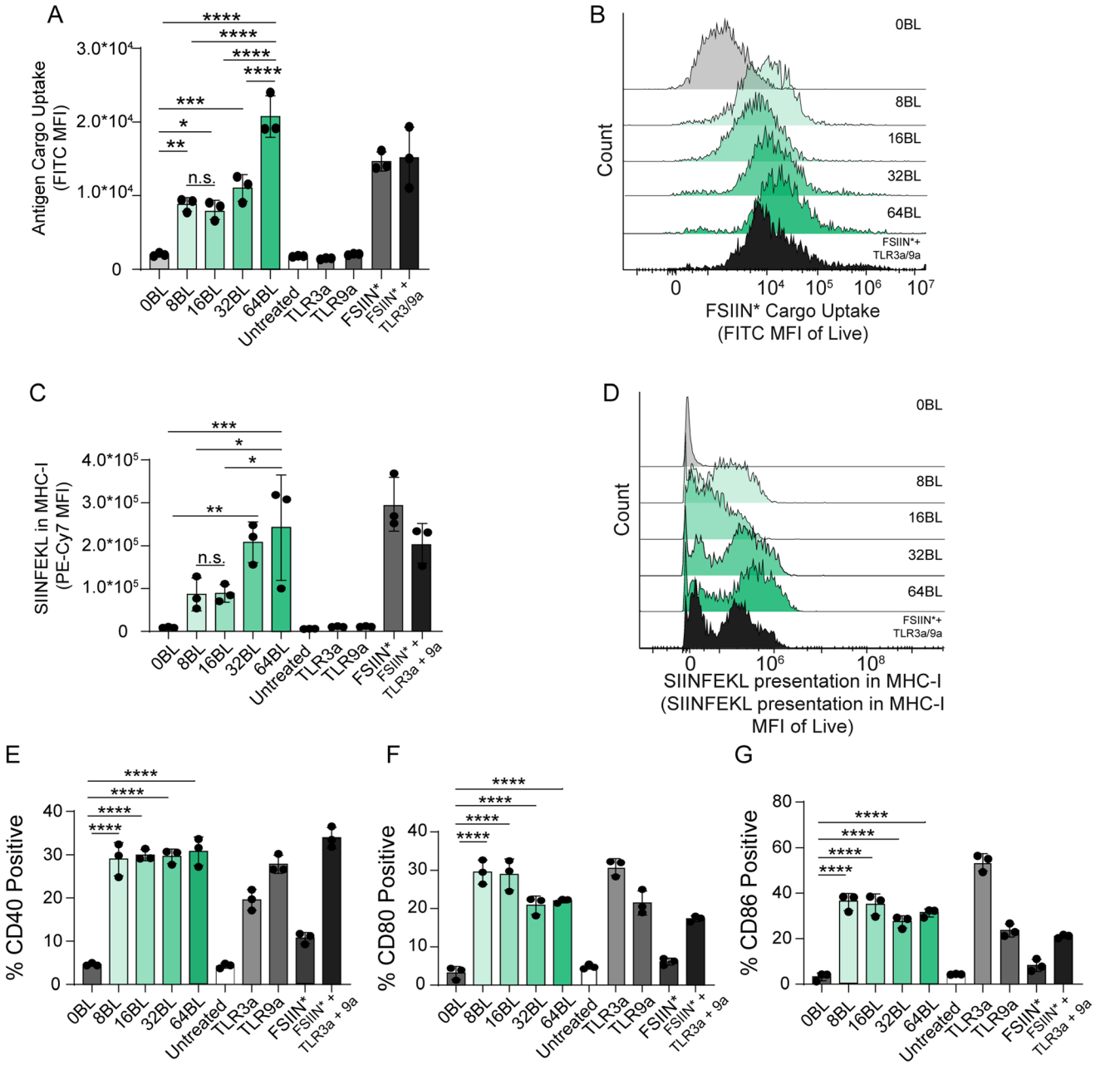

Fig. 3 Altering microneedle loading influences DC cargo uptake and activation. (A) MNA cargo uptake and (B) line traces of FITC-labelled SIINFEKL after treatment with varying-BL 1 : 1 TLR3a : TLR9a MNAs. (C) SIINFEKL presentation and (D) line traces of SIINFEKL presented in MHC1 after treatment with varying-BL MNAs. Frequency of (E) $CD40^+$, (F) $CD80^+$, and (G) $CD86^+$ DCs after treatment with varying-BL MNAs. Data are presented as mean ± SD.

increased antigen-specific effector cell proliferation and improved immune responses; thus, 64 BL-coated needles were chosen for the remainder of cell studies. In all cases MNAs integrating a TLRa drove high levels of DC activation, as evidenced by the frequencies of cells positive for costimulatory markers CD40, CD80, and CD86 (Fig. 3E–G). Excitingly, MNAs coated with all numbers of bilayers generated a costimulatory response that was greater than or equivalent to that of soluble components (statistics not included for the sake of clarity). It is important to note that R9 serves as a cell-penetrating peptide sequence, which may improve uptake of FSIIN* with adjuvants compared to delivery of unmodified SIINFEKL with adjuvants; however, the cationic residues are critical for driving electrostatic assembly of the SIINFEKL antigen with TLRas. Previous work from our lab has shown that this penetrating peptide does facilitate antigen uptake.[46] As such, studies comparing modified with unmodified SIINFEKL and a variety of agonists will need to be conducted to elucidate the immunological importance of this R9 peptide. Application of this coated MNA platform to pathogens whose antigens are

difficult to extract or potentially immunotoxic could be beneficial. For example, MNAs might drive expression of broad activation markers even at small doses (*i.e.*, low numbers of BLs), allowing induction of the same levels of costimulatory marker expression with less antigen.

Combinatorial TLRa MNAs trigger TLR pathways in a composition-dependent manner and promote DC activation

To investigate whether MNAs containing different ratios of TLRas trigger TLR pathways in a composition-dependent manner, we assessed TLR3 and TLR9 signaling in cells treated with 64 BL-MNAs spanning the library of TLR3 and TLR9 ratios used in Fig. 2. Excitingly, in these studies TLR3 signaling was significantly greater in cells treated with MNAs containing higher compositions of TLR3a relative to TLR9a (Fig. 4A); likewise TLR9 signaling was greater in cells treated with designs containing higher compositions of TLR9a relative to TLR3a (Fig. 4B). Inclusion of multiple TLRas activated TLR signaling in cells significantly more than untreated controls. These data confirm the ratio of TLRas assembled with antigen on MNAs controls the relative signaling of distinct TLR pathways. Furthermore, all ratios containing TLR3a activated TLR3 reporter cells significantly more than any single control (statistics not shown for the sake of clarity). This indicates that the codelivery of both antigen and agonist is important for driving a robust DC response. At TLR3a : 9a ratios of 0 : 1, 1 : 2, and 1 : 1, TLR9 reporter cells were activated at similar levels to cells treated with TLR9a only or TLR3a + 9a. These comparisons indicate that for intradermal delivery, this MNA system delivering tunable amounts of cargo could achieve similar immunological outcomes to soluble controls.

We next hypothesized that combinatorial TLRa designs coated with antigen on MNAs would also alter DCs activation profiles relative to MNAs coated with antigen and a single TLRs. To test this, we treated DCs using the same ratio library of MNA coatings and measured cargo uptake, antigen presentation, and costimulatory markers. A gating scheme similar to Fig. 3 was used in the analysis (Fig. S5A†), and viability was analyzed to ensure treatments had minimal impact on cell viability (Fig. S5B†), enabling robust analysis of the surface markers. First, we found that increasing amounts of TLR3a generally increased FSIIN* antigen internalization (Fig. 4C and D), with an increase in uptake at ratios of 1 : 1 TLR3 : 9a and higher. This suggests that the 1 : 1 ratio provides the minimum amount of TLR3a to maximize cargo uptake. Similarly, we found that increasing amounts of TLR3a caused increased SIINFEKL presentation in MHC-I (Fig. 4E and F), as expected from the internalization data above. However, the increase in antigen presentation was more dramatic compared to antigen uptake. This provides further evidence that the system may be especially sensitive to TLR3a, with amounts at the 1 : 1 ratio and higher driving significant antigen uptake and presentation. In examining costimulatory markers, all combinations of TLR3a : TLR9a on MNAs caused a higher percentage of cells to express CD40, CD80, and CD86 markers compared to untreated cells, uncoated MNA-treated cells, or to cells treated with fluorescently- labelled and arginine tagged antigen only (FSIIN*) (Fig. 4G–I). While the soluble controls are not dose-matched to the experimental controls, the comparison of each MNA combination to cells treated with a soluble mixture of FSIIN* and TLR3/9a still provides exciting motivation for future *in vivo* studies using this system. The results in Fig. 4H and I show that all combinations of cues delivered on solid MNAs can activate significantly more DCs to express CD80 and CD86 compared to soluble controls. Furthermore, in the case of CD40 in Fig. 4G, only the 1 : 1 ratio of TLR3 : 9a caused significantly more DCs to express this marker compared to a soluble mixture of all signals with these signals delivered at the same ratio. This result provides motivation for different combinations of TLRas driving differential DC and perhaps other skin-resident immune cell phenotype activation.

As discussed earlier, effector cells require multiple signals to effectively drive an immune response against a particular antigen. In examining specific markers, the 1 : 1 TLR3a : TLR9a caused significantly more cells to express CD40 compared to unequal combinations. CD40 expressed on dendritic cells is an important ligand for the activation of a different subset of effector cells, CD4+ T cells, which interact with other immune cell types to drive robust immunity.[47] While we examined only CD8+ T cells in this work, the tunable expression of CD40 and potentially other surface markers could allow this platform to be applied to diseases where the immune response is mediated by different effector cell subsets. In addition, CD80 and CD86 are upregulated when treated with MNAs containing higher amounts of TLR3a compared to TLR9a. This point is further supported by the comparison to treatment with TLR9a only, where significantly fewer cells expressed these surface markers. This indicates that microneedles coated with higher amounts of TLR3a than TLR9a may induce improved cytotoxic T cell activation, as these markers are implicated in the activation of CD8+ T cells. More broadly, higher percentages of cells expressing specific surface markers when treated with a higher ratio of one TLRa compared to another suggests and opportunity to tune dendritic cell activation. Pathway analysis, for example by qRT-PCR, could reveal differential abilities of these APCs encountering different TLRa ratios to expand and polarize antigen-specific T cells. Toward this goal, we next assessed T cell engagement.

Increased DC activation and antigen availability drives effector cell proliferation

To test if MNAs cause antigen-specific immune cells to proliferate in response to treatment, we cocultured DCs with T cells from transgenic mice in which all CD8+ T cells express T cell receptors for SIINFEKL. These T cells were labelled with a proliferation dye that decreases by half during each successive generation of cell division (Fig. 5A and Fig. S6A†), then analyzed for viability (Fig. S6B†); this revealed the MNA treatments had comparable viability to soluble mixtures. All MNA TLRa compositions caused significant proliferation compared to untreated cells, indicating effective activation of APCs and antigen display in a manner able to expand

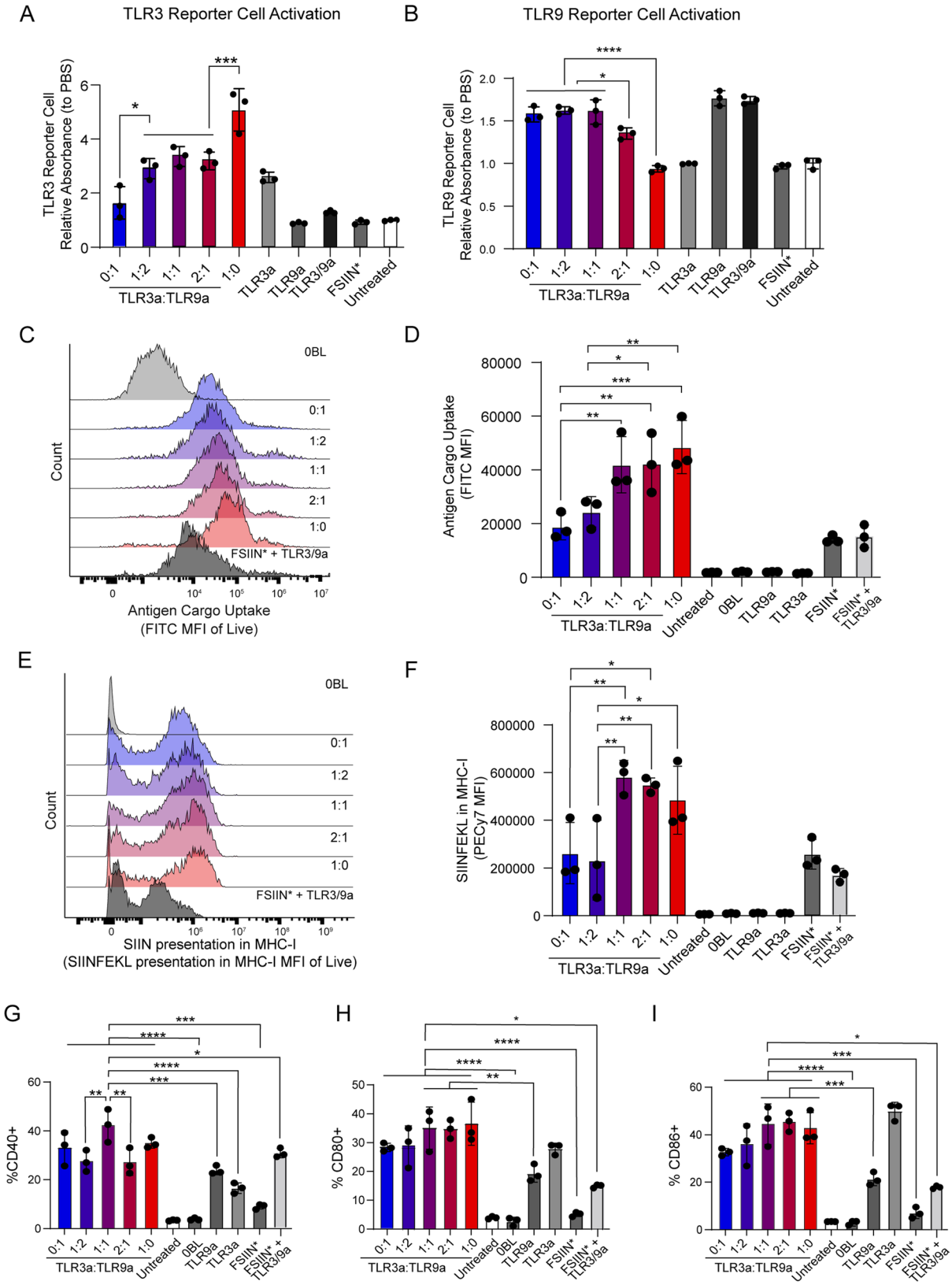

Fig. 4 Microneedles effectively activate DCs towards inflammation using TLR pathways. (A) TLR3 and (B) TLR9 reporter cell activation as a function of MNA composition. Absorbance of SEAP reporter protein was measured and normalized to the amount of SEAP secreted by PBS-treated cells. MNA cargo uptake (C) line traces and (D) MFIs of cargo-positive cells after treatment with varying TLRa MNAs. Antigen presentation (E) line traces and (F) MFIs of cells after treatment with varying TLRa MNAs. Frequency of (G) $CD40^+$, (H) $CD80^+$ and (I) $CD86^+$ DCs after treatment with varying TLRa MNAs. Data are presented as mean ± SD.

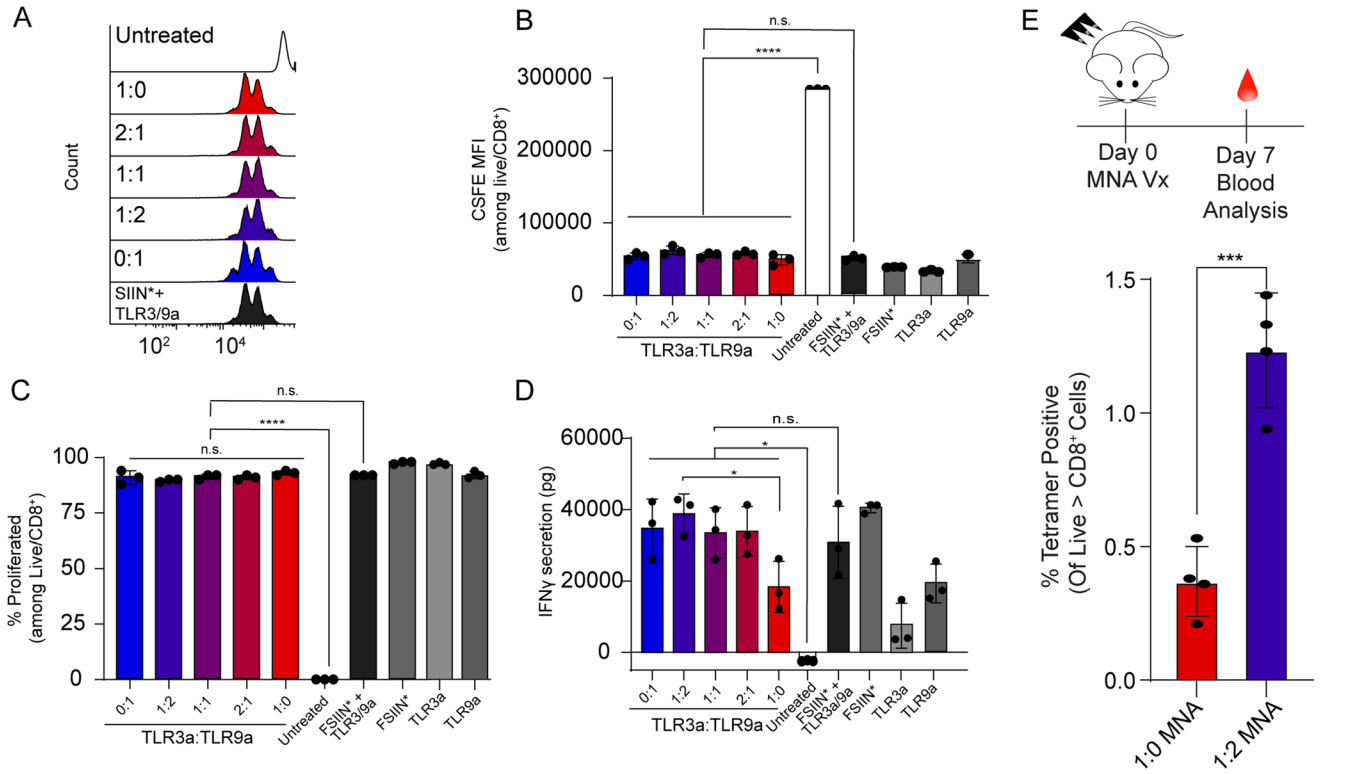

Fig. 5 Increased DC activation and antigen availability drives effector T cell proliferation. T cells were stained CFSE proliferation dye, then co-cultured with DCs and MNA sections. (A) Line traces CFSE signal. Further proliferation is indicated by multiple peaks at lower MFI, quantified in (B). (C) Frequency of cells proliferated past the generation initially added, G0. (D) Quantification of IFNγ. Data are presented as mean ± SD. (E) SIINFEKL MHC-I tetramer measurements on day 7 after mice were vaccinated with the indicated MNA designs. Comparisons are shown between MNA groups, compared to untreated samples, and compared to FSIIN* + TLR3/9a. Comparisons to FSIIN* only, TLR3a only, and TLR9a only are not shown for the sake of clarity.

antigen-specific T cells (Fig. 5B and C). Additionally, all TLRa combinations delivered *via* MNAs caused similar levels of proliferation to soluble delivery of FSIIN* with TLR3/9a. Interestingly, while the level of expansion was similar across TLRa compositions, analyzing the cytokines from the cocultures indicated that T cell function was influenced by TLRa composition. Cytokines determine specific T cell fates as well as function, such as effector response and antibody production. We examined IFNγ, a type 2 IFN, which is produced by antigen-experienced T cells (Fig. 5D). This protein helps to activate macrophages and increases expression of MHC I molecules on APC surfaces. Systemically, IFNγ is an important link between the innate and adaptive immune response.[48,49] All the MNA designs drove IFNγ secretion, but there were some composition-dependent effects—notably higher ratios of TLR9a induced the highest amount of IFNγ (Fig. 5D). This provides interesting contrast to the antigen presentation and costimulatory marker expression in Fig. 4, which were higher in cells treated with higher ratios of TLR3a. Interestingly, IFNγ delivered intradermally has been shown to increase recruitment of $cD11c^+$ DCs to the site of application; understanding how IFNγ is released by these cells in culture may provide important information about the recruitment of immune cells to the site of application.[50] With this in mind, tunable ratios of TLRas set the stage for future studies investigating how modulating TLR signaling with MNAs can be used to generate different responses against the same antigen. Further work will examine how different ratios of TLRas on microneedles cause cells to release additional cytokines, such as IFNα, IFNβ, and interleukins.

$CD8^{\pm}$ T cells responses to vaccination are directed by TLRa compositions in MNAs

As an initial investigation to determine the impact of the number of TLRa components delivered with MNAs, we conducted an *in vivo* mouse vaccine study. In this study we designed MNAs comprising fixed doses of antigen and total TLRa, but different relative TLRa compositions. In particular, cohorts were treated with MNAs containing antigen and single TLRa type, or with MNAs containing antigen and both classes of TLRas. Seven days later we collected peripheral blood and used SIINFEKL MHC-I tetramer staining to quantify the number of $CD8^+$ T cells specific for the vaccine antigen (Fig. 5E, top). Excitingly, while both MNA designs generated measurable tetramer responses, the MNAs containing both classes of TLRa generated significantly higher antigen-specific responses relative to the dose-matched MNAs containing a

single TLRa (Fig. 5E, bottom). These data demonstrate the MNAs are functional, and provides initial data supporting the role of combinatorial classes of TLRa delivered by MNAs in directing antigen-specific T cell immunity.

Conclusions

This work seeks to improve vaccine design and delivery by coating vaccine delivery devices, MNAs, with combinations of TLRas and antigen. We show that cargo adsorption is linearly connected to the number of bilayers deposited, and driven electrostatically. Treating cells with a library of MNAs containing defined ratios of TLR3a : TLR9a reveals that the TLR signal transduction is tunable and defined by MNA composition. This work has implications for future coated microneedle designs by providing multiple tunable parameters to enable desired cargo loading levels and antigen availability. Furthermore, this platform would enable TLRas or other cargo to be placed into distinct layers of the MNA to control the immune response temporally; for example, adding an agonist that binds a receptor expressed at the beginning of cellular infection towards the last few layers (closest to the needle tips) and an agonist that binds a late-infection receptor in the initially-deposited layers (closest to the needle base). In future applications of this MNA design to different disease models, it will be important to study the role of these TLRas on different types of immune cells, such as B cells and CD4+ T cells. Additionally, more comprehensive *in vivo* studies will link modulated APC signaling to effector cell responses with regard to combinations of TLRas, and how these engagements impact functional disease outcomes using this MNA technology.

Author contributions

C. E. and C. M. J. conceived the studies. C. E. and R. S. O. carried out the studies and data analysis. All authors contributed to writing the manuscript. All authors have given approval to the final version of the manuscript.

Abbreviations

TLRa	Toll-like receptor agonist
APC	Antigen presenting cell
TLR	Toll-like receptor
TLR3a	Toll-like receptor 3 agonist
TLR9a	Toll-like receptor 9 agonist
MNA	Microneedle array
DC	Dendritic cell
iPEM	Immune polyelectrolyte multilayer
polyIC	Polyinosinic-polycytidylic
PLLA	Poly(L-lactide)
PDMS	Poly(dimethylsiloxane)
SEM	Scanning electron microscopy
BL	bilayers
FSIIN*	FITC SIINFEKL-R9
BL	Bilayers
CFSE	Carboxyfluorescein succinimidyl ester.

Conflicts of interest

C. M. J. is an employee of the VA Maryland Health Care System. C. M. J. has equity positions with Cartesian Therapeutics and Vaccitech, plc. The remaining authors declare that the research was conducted in the absence of any commercial or financial relationships that could be construed as a potential conflict of interest.

Acknowledgements

This work was supported by the National Institutes of Health Award # R01EB027143 and # R01AI144667 to C. M. J. C. E. was supported in part by the Clark Doctoral Fellowship from the Clark School of Engineering, University of Maryland, College Park and by a National Institute of Health Training Grant (Award # 2T32CA154274-11A1). R. S. O. was supported in part by Veterans Affairs Career Development Award (IK2 BX005061). Some data in this manuscript were attained using instruments in the BioWorkshop core facility in the Fischell Department of Bioengineering at the University of Maryland, College Park. We would like to thank Dr Sijie Hao, the manager of the core facility, for providing training and technical assistance. The TOC graphic was created using Biorender.com.

References

1 A. Ghosh and L. Dar, Dengue vaccines: challenges, development, current status and prospects, *Indian J. Med. Microbiol.*, 2015, **33**, 3–15, DOI: **10.4103/0255-0857.148369**.
2 P. M. Heaton, Challenges of Developing Novel Vaccines With Particular Global Health Importance, *Front. Immunol.*, 2020, **11**, 517290, DOI: **10.3389/fimmu.2020.517290**.
3 S. J. Tsai, S. K. Black and C. M. Jewell, Leveraging the modularity of biomaterial carriers to tune immune responses, *Adv. Funct. Mater.*, 2020, **30**, 2004119, DOI: **10.1002/adfm.202004119**.
4 M. A. Anwar, M. Shah, J. Kim and S. Choi, Recent clinical trends in Toll-like receptor targeting therapeutics, *Med. Res. Rev.*, 2019, **39**, 1053–1090, DOI: **10.1002/med.21553**.
5 M. Smith, *et al.*, Trial Watch: Toll-like receptor agonists in cancer immunotherapy, *OncoImmunology*, 2018, **7**, e1526250, DOI: **10.1080/2162402X.2018.1526250**.
6 A. H. Forster, *et al.*, Safety, tolerability, and immunogenicity of influenza vaccination with a high-density microarray patch: Results from a randomized, controlled phase I clinical trial, *PLoS Med.*, 2020, **17**, e1003024, DOI: **10.1371/journal.pmed.1003024**.

7 P. M. Frew, *et al.*, Acceptability of an inactivated influenza vaccine delivered by microneedle patch: Results from a phase I clinical trial of safety, reactogenicity, and immunogenicity, *Vaccine*, 2020, **38**, 7175–7181, DOI: **10.1016/j.vaccine.2020.07.064**.
8 T. L. Murphy and K. M. Murphy, Dendritic cells in cancer immunology, *Cell. Mol. Immunol.*, 2021, DOI: **10.1038/s41423-021-00741-5**.
9 A. H. Hovav, Dendritic cells of the oral mucosa, *Mucosal Immunol.*, 2014, **7**, 27–37, DOI: **10.1038/mi.2013.42**.
10 S. Y. Chang, H. J. Ko and M. N. Kweon, Mucosal dendritic cells shape mucosal immunity, *Exp. Mol. Med.*, 2014, **46**, e84, DOI: **10.1038/emm.2014.16**.
11 C. W. Cutler and R. Jotwani, Dendritic cells at the oral mucosal interface, *J. Dent. Res.*, 2006, **85**, 678–689, DOI: **10.1177/154405910608500801**.
12 Q. Zeng, J. M. Gammon, L. H. Tostanoski, Y. C. Chiu and C. M. Jewell, In Vivo Expansion of Melanoma-Specific T Cells Using Microneedle Arrays Coated with Immune-Polyelectrolyte Multilayers, *ACS Biomater. Sci. Eng.*, 2017, **3**, 195–205, DOI: **10.1021/acsbiomaterials.6b00414**.
13 Q. Zeng and C. M. Jewell, Directing toll-like receptor signaling in macrophages to enhance tumor immunotherapy, *Curr. Opin. Biotechnol*, 2019, **60**, 138–145, DOI: **10.1016/j.copbio.2019.01.010**.
14 C. Petitdemange, *et al.*, Vaccine induction of antibodies and tissue-resident CD8+ T cells enhances protection against mucosal SHIV-infection in young macaques, *JCI Insight*, 2019, **4**(4), e126047, DOI: **10.1172/jci.insight.126047**.
15 A. M. Krieg, Therapeutic potential of Toll-like receptor 9 activation, *Nat. Rev. Drug Discovery*, 2006, **5**, 471–484, DOI: **10.1038/nrd2059**.
16 H. Kanzler, F. J. Barrat, E. M. Hessel and R. L. Coffman, Therapeutic targeting of innate immunity with Toll-like receptor agonists and antagonists, *Nat. Med.*, 2007, **13**, 552–559, DOI: **10.1038/nm1589**.
17 T. Kaisho and S. Akira, Toll-like receptor function and signaling, *J. Allergy Clin. Immunol.*, 2006, **117**, 979–987, DOI: **10.1016/j.jaci.2006.02.023**, quiz 988.
18 G. J. Nau, *et al.*, Human macrophage activation programs induced by bacterial pathogens, *Proc. Natl. Acad. Sci. U. S. A.*, 2002, **99**, 1503–1508, DOI: **10.1073/pnas.022649799**.
19 E. Froimchuk, R. S. Oakes, S. M. Kapnick, A. A. Yanes and C. M. Jewell, Biophysical Properties of Self-Assembled Immune Signals Impact Signal Processing and the Nature of Regulatory Immune Function, *Nano Lett.*, 2021, **21**, 3762–3771, DOI: **10.1021/acs.nanolett.0c05118**.
20 J. R. Teijaro and D. L. Farber, COVID-19 vaccines: modes of immune activation and future challenges, *Nat. Rev. Immunol.*, 2021, **21**, 195–197, DOI: **10.1038/s41577-021-00526-x**.
21 W. H. Kruit, *et al.*, Immunization with recombinant MAGE-A3 protein combined with adjuvant systems AS15 or AS02B in patients with unresectable and progressive metastatic cutaneous melanoma: A randomized open-label phase II study of the EORTC Melanoma Group (16032-18031), *J. Clin. Oncol.*, 2008, **26**, 9065–9065, DOI: **10.1200/jco.2008.26.15_suppl.9065**.
22 T. Kawasaki and T. Kawai, Toll-like receptor signaling pathways, *Front. Immunol.*, 2014, **5**, 461, DOI: **10.3389/fimmu.2014.00461**.
23 S. G. Reed, M. T. Orr and C. B. Fox, Key roles of adjuvants in modern vaccines, *Nat. Med.*, 2013, **19**, 1597–1608, DOI: **10.1038/nm.3409**.
24 S. P. Kasturi, *et al.*, Programming the magnitude and persistence of antibody responses with innate immunity, *Nature*, 2011, **470**, 543–547, DOI: **10.1038/nature09737**.
25 A. Ullah, *et al.*, Microneedle array with a pH-responsive polymer coating and its application in smart drug delivery for wound healing, *Sens. Actuators, B*, 2021, **345**, 130441, DOI: **10.1016/j.snb.2021.130441**.
26 Y. C. Kim, J. H. Park and M. R. Prausnitz, Microneedles for drug and vaccine delivery, *Adv. Drug Delivery Rev.*, 2012, **64**, 1547–1568, DOI: **10.1016/j.addr.2012.04.005**.
27 M. L. Bookstaver, S. J. Tsai, J. S. Bromberg and C. M. Jewell, Improving Vaccine and Immunotherapy Design Using Biomaterials, *Trends Immunol.*, 2018, **39**, 135–150, DOI: **10.1016/j.it.2017.10.002**.
28 M. E. Turvey, *et al.*, Microneedle-based intradermal delivery of stabilized dengue virus, *Bioeng. Transl. Med.*, 2019, **4**, e10127, DOI: **10.1002/btm2.10127**.
29 Y. C. Kim, *et al.*, Fabrication of microneedle patches with lyophilized influenza vaccine suspended in organic solvent, *Drug Delivery Transl. Res.*, 2021, **11**, 692–701, DOI: **10.1007/s13346-021-00927-4**.
30 S. Henry, D. V. McAllister, M. G. Allen and M. R. Prausnitz, Microfabricated microneedles: a novel approach to transdermal drug delivery, *J. Pharm. Sci.*, 1998, **87**, 922–925, DOI: **10.1021/js980042+**.
31 M. R. Prausnitz and R. Langer, Transdermal drug delivery, *Nat. Biotechnol.*, 2008, **26**, 1261–1268, DOI: **10.1038/nbt.1504**.
32 C. M. C. Rodrigues and S. A. Plotkin, Impact of Vaccines; Health, Economic and Social Perspectives, *Front. Microbiol.*, 2020, **11**, 1526, DOI: **10.3389/fmicb.2020.01526**.
33 C. Caudill, *et al.*, Transdermal vaccination via 3D-printed microneedles induces potent humoral and cellular immunity, *Proc. Natl. Acad. Sci. U. S. A.*, 2021, **118**, DOI: **10.1073/pnas.2102595118**.
34 F. Arikat, *et al.*, Targeting proinsulin to local immune cells using an intradermal microneedle delivery system; a potential antigen-specific immunotherapy for type 1 diabetes, *J. Controlled Release*, 2020, **322**, 593–601, DOI: **10.1016/j.jconrel.2020.02.031**.
35 L. Yenkoidiok-Douti, C. Barillas-Mury and C. M. Jewell, Design of Dissolvable Microneedles for Delivery of a Pfs47-Based Malaria Transmission-Blocking Vaccine, *ACS Biomater. Sci. Eng.*, 2021, **7**, 1854–1862, DOI: **10.1021/acsbiomaterials.0c01363**.
36 M. Dalvi, *et al.*, Panorama of dissolving microneedles for transdermal drug delivery, *Life Sci.*, 2021, **284**, 119877, DOI: **10.1016/j.lfs.2021.119877**.

37 N. G. Rouphael, *et al.*, The safety, immunogenicity, and acceptability of inactivated influenza vaccine delivered by microneedle patch (TIV-MNP 2015): a randomised, partly blinded, placebo-controlled, phase 1 trial, *Lancet*, 2017, **390**, 649–658, DOI: **10.1016/s0140-6736(17)30575-5**.

38 S. P. Sullivan, *et al.*, Dissolving polymer microneedle patches for influenza vaccination, *Nat. Med.*, 2010, **16**, 915–920, DOI: **10.1038/nm.2182**.

39 C. E. Chandler, *et al.*, *In Vivo* Intradermal Delivery of Bacteria by Using Microneedle Arrays, *Infect. Immun.*, 2018, **86**, DOI: **10.1128/IAI.00406-18**.

40 R. S. Oakes, *et al.*, Exploiting Rational Assembly to Map Distinct Roles of Regulatory Cues during Autoimmune Therapy, *ACS Nano*, 2021, **15**, 4305–4320, DOI: **10.1021/acsnano.0c07440**.

41 L. H. Tostanoski, *et al.*, Design of Polyelectrolyte Multilayers to Promote Immunological Tolerance, *ACS Nano*, 2016, **10**, 9334–9345, DOI: **10.1021/acsnano.6b04001**.

42 M. L. Bookstaver, *et al.*, Self-Assembly of Immune Signals to Program Innate Immunity through Rational Adjuvant Design, *Adv. Sci.*, 2022, e2202393, DOI: **10.1002/advs.202202393**.

43 H. B. Eppler and C. M. Jewell, Biomaterials as Tools to Decode Immunity, *Adv. Mater.*, 2020, **32**, e1903367, DOI: **10.1002/adma.201903367**.

44 S. A. Shah, R. S. Oakes, S. M. Kapnick and C. M. Jewell, Mapping the Mechanical and Immunological Profiles of Polymeric Microneedles to Enable Vaccine and Immunotherapy Applications, *Front. Immunol.*, 2022, **13**, DOI: **10.3389/fimmu.2022.843355**.

45 P. C. DeMuth, *et al.*, Polymer multilayer tattooing for enhanced DNA vaccination, *Nat. Mater.*, 2013, **12**, 367–376, DOI: **10.1038/nmat3550**.

46 M. L. Bookstaver, K. L. Hess and C. M. Jewell, Self-Assembly of Immune Signals Improves Codelivery to Antigen Presenting Cells and Accelerates Signal Internalization, Processing Kinetics, and Immune Activation, *Small*, 2018, **14**, 1802202, DOI: **10.1002/smll.201802202**.

47 A. Chatzigeorgiou, M. Lyberi, G. Chatzilymperis, A. Nezos and E. Kamper, CD40/CD40L signaling and its implication in health and disease, *Biofactors*, 2009, **35**, 474–483, DOI: **10.1002/biof.62**.

48 A. J. Lee and A. A. Ashkar, The Dual Nature of Type I and Type II Interferons, *Front. Immunol.*, 2018, **9**, DOI: **10.3389/fimmu.2018.02061**.

49 T. J. Kindt, R. A. Goldsby, B. A. Osborne and J. Kuby, *Kuby Immunology*, ed. T. J. Kindt, R. A. Goldsby and B. A. Osborne, W.H. Freeman, New York, 6th edn, c2007, 2003.

50 L. M. Johnson-Huang, *et al.*, A single intradermal injection of IFN-gamma induces an inflammatory state in both non-lesional psoriatic and healthy skin, *J. Invest. Dermatol.*, 2012, **132**, 1177–1187, DOI: **10.1038/jid.2011.458**.